



# A two-step model for dynamical dike propagation in two dimensions: Application to the July 2001 Etna eruption

V. Pinel, A. Carrara, F. Maccaferri, E. Rivalta, F. Corbi

## ► To cite this version:

V. Pinel, A. Carrara, F. Maccaferri, E. Rivalta, F. Corbi. A two-step model for dynamical dike propagation in two dimensions: Application to the July 2001 Etna eruption. *Journal of Geophysical Research: Solid Earth*, 2017, 122, pp.1107-1125. 10.1002/2016JB013630 . insu-03661353

HAL Id: insu-03661353

<https://insu.hal.science/insu-03661353>

Submitted on 6 May 2022

**HAL** is a multi-disciplinary open access archive for the deposit and dissemination of scientific research documents, whether they are published or not. The documents may come from teaching and research institutions in France or abroad, or from public or private research centers.

Copyright

L'archive ouverte pluridisciplinaire **HAL**, est destinée au dépôt et à la diffusion de documents scientifiques de niveau recherche, publiés ou non, émanant des établissements d'enseignement et de recherche français ou étrangers, des laboratoires publics ou privés.

# Journal of Geophysical Research: Solid Earth

## RESEARCH ARTICLE

10.1002/2016JB013630

**Key Points:**

- Numerical model solving in 2-D for magma path and velocity is presented
- Surface loading attracts the magma and reduces its velocity
- Surface unloading diverts the magma to peripheral eruptive vents retarding the eruption

**Correspondence to:**V. Pinel,  
Virginie.Pinel@univ-smb.fr**Citation:**

Pinel, V., A. Carrara, F. Maccaferri, E. Rivalta, and F. Corbi (2017), A two-step model for dynamical dike propagation in two dimensions: Application to the July 2001 Etna eruption, *J. Geophys. Res. Solid Earth*, 122, 1107–1125, doi:10.1002/2016JB013630.

Received 7 OCT 2016

Accepted 29 JAN 2017

Accepted article online 3 FEB 2017

Published online 25 FEB 2017

## A two-step model for dynamical dike propagation in two dimensions: Application to the July 2001 Etna eruption

V. Pinel<sup>1</sup>, A. Carrara<sup>1</sup>, F. Maccaferri<sup>2</sup>, E. Rivalta<sup>2</sup>, and F. Corbi<sup>2,3</sup><sup>1</sup>ISTerre, IRD, CNRS, Université Savoie Mont-Blanc, Le Bourget du Lac, France, <sup>2</sup>GFZ German Centre for Geosciences, Potsdam, Germany, <sup>3</sup>Géosciences Montpellier Laboratory, University of Montpellier, Montpellier, France

**Abstract** We developed a hybrid numerical model of dike propagation in two dimensions solving both for the magma trajectory and velocity as a function of the source overpressure, the magma physical properties (density and viscosity), and the crustal density and stress field. This model is used to characterize the influence of surface load changes on magma migration toward the surface. We confirm that surface loading induced by volcanic edifice construction tends both to attract the magma and to reduce its velocity. In contrast, surface unloading, for instance, due to caldera formation, tends to divert the magma to the periphery-retarding eruption. In both cases the deflected magma may remain trapped at depth. Amplitudes of dike deflection and magma velocity variation depend on the ratio between the magma driving pressure (source overpressure as well as buoyancy) and the stress field perturbation. Our model is then applied to the July 2001 eruption of Etna, where the final dike deflection had been previously interpreted as due to the topographic load. We show that the velocity decrease observed during the last stage of the propagation can also be attributed to the local stress field. We use the dike propagation duration to estimate the magma overpressure at the dike bottom to be less than 4 MPa. This approach can be potentially used to forecast if, where, and when propagating magma might reach the surface when having knowledge on the local stress field, magma physical properties, and reservoir overpressure.

### 1. Introduction

Basaltic eruptions are often fed by magmatic intrusions that propagate through the crust for a few hours to a few days before reaching the surface. Geodetic and seismic signals induced by magma propagation recorded before recent eruptions have illustrated with unprecedented detail nonstraight magma pathways [Sigmundsson *et al.*, 2014; Cannavò *et al.*, 2015]. When dikes do not follow a preexisting fault, they tend to orient perpendicular to the least compressive principal stress [Anderson, 1951; Cotterell and Rice, 1980; Delaney *et al.*, 1986], and this behavior has long been used to derive the local stress field directions from field observations [Nakamura *et al.*, 1977; Chaput *et al.*, 2013]. However, dikes require some time and therefore some distance to adjust to the local stress field [Menand *et al.*, 2010], so that the knowledge of the principal stress orientation alone may not be enough to forecast the orientation of dikes and vice versa. The stress field may be strongly deviatoric at the spatial scale of a volcanic edifice, e.g., due to the edifice load [Accocella and Tibaldi, 2005] or activity of preexisting faults [Xu *et al.*, 2015]. Moreover, the velocity of propagation is not constant over time [Peltier *et al.*, 2007; Sigmundsson *et al.*, 2014]. Many dikes become permanently trapped before they intersect the surface [Pedersen *et al.*, 2006; Roult *et al.*, 2012]; other may become temporarily arrested and resume propagation upon additional magma supply [Sigmundsson *et al.*, 2014].

In terms of hazard and risk assessment it is crucial to be able to forecast whether a propagating dike will make it to the surface and end in an eruption. In case an eruption is expected, a forecast of the potential vent location would also be desirable, as the human and economic impact depends on the distribution of population and infrastructure. In addition, the explosivity of an eruption may depend on the location of the vent, due to interaction of magma with ice or water [Sigmundsson *et al.*, 2010]. Information on the expected timing of the eruption may also help mitigate its impact.

Dike pathways and velocity depend on many factors, including (i) the location of the magma source, its geometry, and physical state; (ii) the physical properties of magma; (iii) the physical properties of country rocks; and (iv) the regional and local stress field. For example, numerical and analog models have shown that ascending dikes approaching a volcanic edifice become deflected on their pathway [Watanabe *et al.*, 1999;

Dahm, 2000a; Muller et al., 2001; Watanabe et al., 2002; Maccaferri et al., 2011; Corbi et al., 2016] and decelerate [Pinel and Jaupart, 2000; Watanabe et al., 2002; Maccaferri et al., 2016; Corbi et al., 2016]. The deflection is oriented toward the center of the surface load, and its amplitude depends on the ratio between the applied load and the magma driving pressure (deflection increases for larger surface load) [Watanabe et al., 1999; Muller et al., 2001; Watanabe et al., 2002]. More recently, the control exerted on dike trajectories by unloading due to mass wasting events or crustal thinning has also been evidenced [Maccaferri et al., 2014; Corbi et al., 2015, 2016]. Similarly, the effect of a compressive stress on the deflection of a vertically ascending dike into a horizontal sill depends on the ratio between the amplitude of the deviatoric stress over the buoyancy forces [Menand et al., 2010].

Magma migration below a volcanic edifice is a complex, nonsteady state process. Forecast tools for dike propagation need to answer three key questions: if, where, and when magma will reach the surface. To this purpose, models need to be integrated with geophysical observations. However, current numerical models for dike propagation are still too rudimentary to answer simultaneously all these questions. This is because most models belong to either one of two end-member categories, the so-called viscosity-dominated and fracturing-dominated regimes, that drastically simplify the magma migration problem to make it mathematically solvable [Rivalta et al., 2015]. Viscosity-dominated regime models are dynamical models able to quantify velocity changes of propagating cracks due to dynamic changes in the magma source or due to variations of the crustal properties or stress field [Mériaux and Jaupart, 1998; Pinel and Jaupart, 2000, 2004; Taisne and Jaupart, 2009; Traversa et al., 2010]. However, these models assume a straight propagation and are thus unable to output the expected magma pathway. On the other hand, fracturing-dominated regime models allow solution for the dike trajectory based on fracturing or energetic criteria by considering the external stress field, host rock properties, magma density, and compressibility [Dahm, 2000a; Muller et al., 2001; Mériaux and Lister, 2002; Maccaferri et al., 2011; Heimisson et al., 2015]. The main limitation of these models is neglecting, or drastically approximating, the effect of viscous pressure loss due to magma flow in the pressure budget within the propagating crack [Dahm, 2000a; Maccaferri et al., 2011; Mériaux and Lister, 2002]. These models thus cannot provide any direct information on the dike velocity, which is controlled by the viscous flow in the crack.

Two-dimensional models able to account simultaneously for the dynamics of the viscous fluid (Navier-Stokes equations) and the fracturing process at the dike tip are still a challenge from a theoretical and numerical point of view and limited to a few attempts that still assume straight propagation [Dahm, 2000b; Roper and Lister, 2007]. An interesting approach has recently been provided by Zhang et al. [2014], who included dike interaction with both the local stress field and the magma flow. However, they did not include the effect of magma buoyancy on the magma pathway. They also did not consider the actual stress field variations acting on the dike along the deflected magma trajectory.

In this paper, we aim at making a first step toward developing a comprehensive model for dike propagation integrating a trajectory estimation and considering the influence of the magma flow. We present a two-step model of dike propagation, which consists in first retrieving the 2-D dike trajectory and then running a 1-D dynamical model of dike propagation along the trajectory retrieved in Step 1. With this approach we characterize how a given surface load distribution influences magma migration toward the surface. We consider two opposite cases of surface loading: edifice construction (loading) and mass wasting due to caldera or flank collapse (unloading). Next, we apply our model to the July 2001 flank eruption at Mount Etna. Finally, we discuss model limitations and potential improvements, before describing the perspectives offered by this new conceptual modeling tool.

## 2. Model Description

We consider a local stress field due to surface loading/unloading and crustal stress (here extension). The stress field can be calculated analytically or numerically. For instance, we use the 2-D plane strain analytical expressions for the stress field induced by a uniform pressure  $P_{\text{load}}$  applied at the surface of a half-space over a segment  $2L_{\text{load}}$  [Watanabe et al., 2002]. Surface unloading can be computed applying a negative pressure  $P_{\text{load}} < 0$ .

### 2.1. Step 1: Trajectory Calculation

We determine the magma trajectory, defined as a curvilinear coordinate corresponding to given spatial position,  $x(s)$  and  $z(s)$  with  $s = 0$  at the dike bottom (depth  $z = H$ ) corresponding to the location of the pressurized

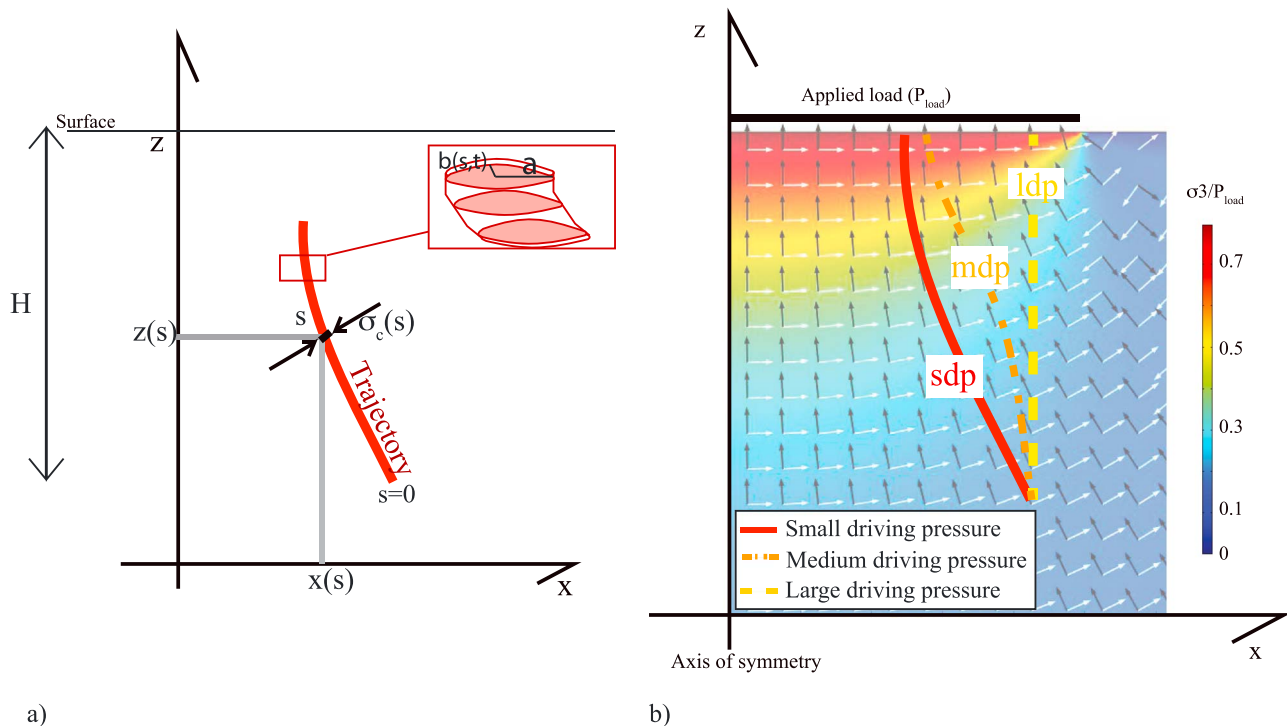


**Figure 1.** Schematic representation of the dike trajectory. (a) Curvilinear coordinate and associated normal stress field  $\sigma_c$  applied on a dike opening along the trajectory. Inset shows the dike elliptical cross section with constant half-breadth  $a$  and half-thickness  $b(s, t)$ . (b) Schematic trajectories for the various cases. When the magma driving pressure is small compared to the deviatoric stress field (small driving pressure case), the trajectory follows the principal stress  $\sigma_1$ ; when the magma driving pressure is large compared to the deviatoric stress field (large driving pressure case), the trajectory is vertical. For intermediate magma driving pressure (medium driving pressure case), the trajectory is located in between the two end-members trajectories. The background is the stress field induced by a cylindrical load applied on a homogeneous elastic half-space derived analytically from Sneddon [1951]. Black and white arrows are, respectively, for the orientation of  $\sigma_1$  and  $\sigma_3$ . The color scale is for the amplitude of  $\sigma_3$  normalized by the applied load.

magma storage (Figure 1a). Analog experiments [Watanabe *et al.*, 1999; Muller *et al.*, 2001; Watanabe *et al.*, 2002] and 2-D numerical calculations [Dahm, 2000a; Muller *et al.*, 2001; Mériaux and Lister, 2002; Kühn and Dahm, 2004; Maccaferri *et al.*, 2011] have shown that the dikes take some distance to align along  $\sigma_1$ , depending on the relative competition between the internal magma driving pressure and the deviatoric stress field. Hence, the expected pathway will be closely aligned to  $\sigma_1$  for a small driving pressure (this case will be labeled in the following as *sdp*) and it will be straight vertical for large driving pressure (labeled as *ldp*). A driving pressure intermediate between the two end-member cases (*mdp*) will result in an intermediate pathway (Figure 1b).

A full calculation of the trajectory requires a static numerical model for dike propagation in 2-D. Available models are based on a criterium for mode I fracturation [Mériaux and Lister, 2002] or an equivalent energy criterium [Dahm, 2000a; Maccaferri *et al.*, 2011]. Here we use the 2-D, boundary element (BE) model developed by Maccaferri *et al.* [2011], where the dike pathway is selected by maximizing the strain plus gravitational energy released by the dike on incremental propagations along different test directions.

This model assumes a constant amount of compressible magma which propagates upward driven by the magma buoyancy. The mass conservation is obtained by accounting for the magma density changes induced by the crack volume changes [Dahm, 2000a; Maccaferri *et al.*, 2011]. In such conditions, the average dike over-pressure can be estimated as follows:  $p_m = (\rho_c - \rho_m)gL_z/4$ , where  $L_z$  is the crack vertical extension [Watanabe *et al.*, 2002]. The initial crack length is chosen so that the stress intensity factor at the deeper dike edge vanishes. Trajectories are calculated for an initially vertical crack.

We also calculate the amplitude of the stress component normal to this trajectory,  $\sigma_c(s)$ , which corresponds to the stress the magma pressure has to counterbalance for the dike to open (Figure 1a).

## 2.2. Step 2: Dynamical Propagation Along the Trajectory

Next, we consider a magma-filled fracture propagating along the trajectory defined in Step 1. The dike cross section on a plane perpendicular to the trajectory is taken as an ellipse of constant half-breadth  $a$ . We solve for the opening (ellipse semiaxis,  $b$ ) as a function of the time and the coordinate along the trajectory. Following *Lister* [1990a, 1990b], we neglect the strength of the surrounding rocks and focus on the balance between buoyancy, viscous pressure, and elastic stresses. We adapt the method described in *Pinel and Jaupart* [2000] to account for a curvilinear trajectory.

The balance of the stresses perpendicular to the dike plane can be expressed as follows:

$$\Delta\sigma(s, t) = \Delta P_o + (\rho_c - \rho_m)g[z(s) - z_{(s=0)}] - \sigma_c(s) + p, \quad (1)$$

where  $\Delta\sigma$  is the magma overpressure,  $\Delta P_o$  is the magma overpressure at the dike bottom, corresponding to the reservoir overpressure,  $\rho_c$  and  $\rho_m$  are the density of the crust and magma (here assumed to be uniform), respectively,  $\sigma_c$  is the component perpendicular to the dike wall of the confining stress field, and  $p$  is the viscous pressure drop induced by the flow ( $p$  being equal to zero for a static dike).

A dike opens provided that the internal magma pressure exceeds the confining stress ( $\Delta\sigma > 0$ ). Then, as long as  $b(s, t) << a$ , the opening is proportional to  $\Delta\sigma$  [*Muskhelishvili*, 1963]

$$\Delta\sigma(s, t) \approx \frac{G}{1 - \nu} \frac{b(s, t)}{a}, \quad (2)$$

with  $G$  the crustal rigidity and  $\nu$  the Poisson's ratio.

Considering the magma as a Newtonian, viscous, and incompressible fluid in a laminar regime, the continuity equation can be expressed as follows [*Pinel and Jaupart*, 2000]:

$$\frac{\partial b(s, t)}{\partial t} = \frac{1}{4\mu} \frac{\partial}{\partial s} \left( b^3(s, t) \frac{\partial p}{\partial s} \right), \quad (3)$$

with  $\mu$  magma viscosity.

Combining equations (1), (2), and (3), we obtain the following differential equation for  $b$ :

$$\frac{\partial b(s, t)}{\partial t} = \frac{G}{16\mu a(1 - \nu)} \frac{\partial^2 b^4}{\partial s^2} + \frac{1}{4\mu} \frac{\partial}{\partial s} \left[ \left( \frac{\partial \sigma_c}{\partial s} - (\rho_c - \rho_m)g \frac{\partial z}{\partial s} \right) b^3 \right]. \quad (4)$$

We scale the pressures by the overpressure at the dike bottom,  $\Delta P_o$ , and the distance along the dike trajectory by  $H$ . Scales for time and fracture opening are given by

$$[t] = \frac{16\mu H^2 G^2}{\Delta P_o^3 a^2 (1 - \nu)^2}, \quad (5)$$

$$[b] = \frac{\Delta P_o a (1 - \nu)}{G}. \quad (6)$$

The system is characterized by a dimensionless number  $N_1 = ((\rho_c - \rho_m)gH)/\Delta P_o$  comparing the maximum buoyancy force (for a dike length  $H$ ) with the magma source overpressure. *Traversa et al.* [2010] have shown that, in case of a constant bottom overpressure, the magma inflow at the dike bottom remains constant through time provided that  $N_1$  is large enough (for  $N_1 > 3.5$ ). The dimensionless expression corresponding to equation (4) is then

$$\frac{\partial b(s, t)}{\partial t} = \frac{\partial^2 b^4}{\partial s^2} + 4 \frac{\partial}{\partial s} \left[ \left( \frac{\partial \sigma_c}{\partial s} - N_1 \frac{\partial z}{\partial s} \right) b^3 \right]. \quad (7)$$

We consider three additional dimensionless numbers:  $N_2 = (\Delta P_o + (\rho_c - \rho_m)gH)/P_{load} = P_m/P_{load} = \Delta P_o(1 + N_1)/P_{load}$ , which compares the total magma driving pressure with the applied load,  $Z_{in}^* = |z_{(s=0)}|/L_{load} = H/L_{load}$  and  $X_{in}^* = x_{(s=0)}/L_{load}$  both characterizing the starting position of the dike within the stress field induced by the load.

Equation (7) is solved numerically using a semi-implicit finite difference scheme applying a fixed dike opening at the bottom (Dirichlet condition), which corresponds to considering a constant reservoir overpressure at the dike bottom. We initiate the calculation with a parabolic profile for the dike opening over 1% of the total

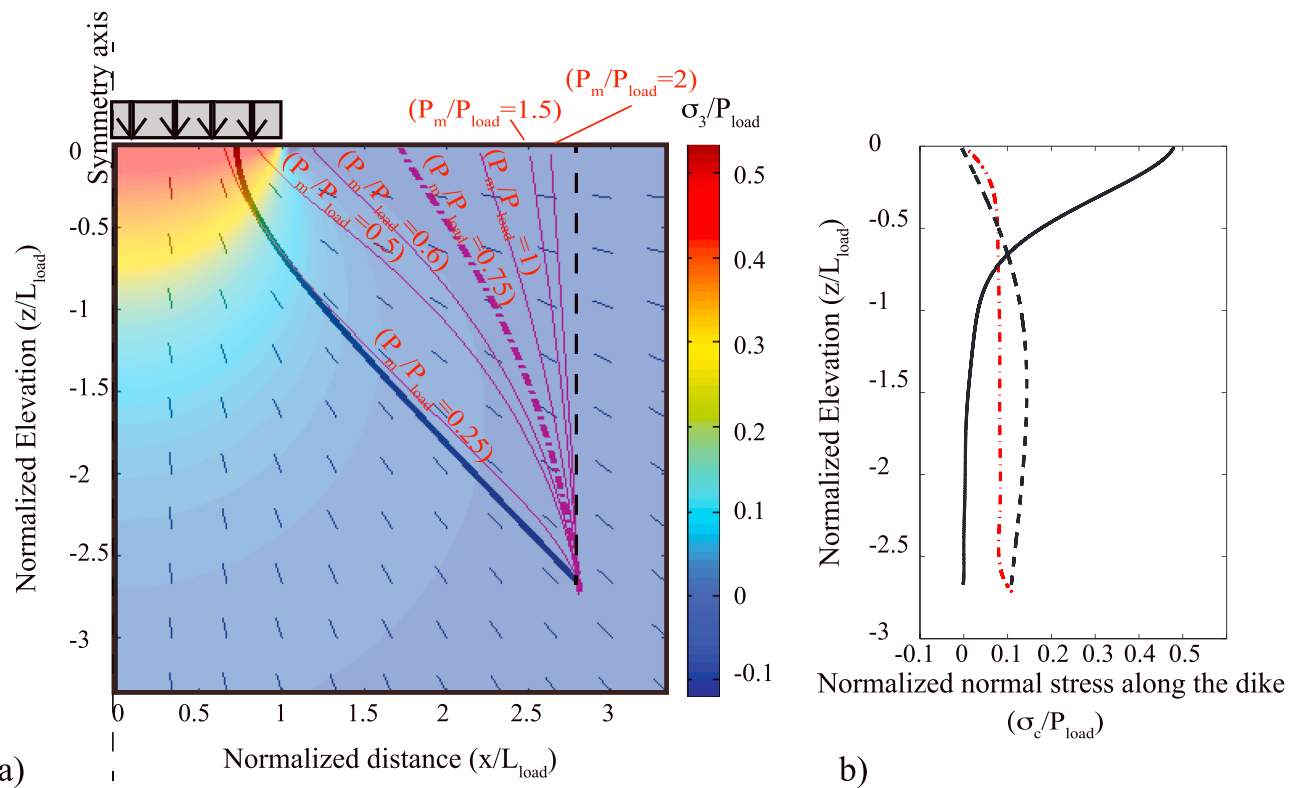


**Figure 2.** Dike trajectories in a crust loaded at the surface. (a) Stress induced by a load  $P_{\text{load}}$  applied at the surface of a homogeneous elastic medium over a segment  $2L_{\text{load}}$  (similar to Figure 1 b but in 2-D plane strain approximation). Black lines are for the orientation of  $\sigma_1$ . The color scale is for the amplitude of  $\sigma_3$ . The plain line is the path of a dike starting at a normalized depth of 2.7 and a normalized radial distance of 2.8 from the axis of the load (similar to the setup described in Figure 5b of Watanabe *et al.* [2002]) and following  $\sigma_1$  (small driving pressure case); the dashed line is the path of a vertical dike (large driving pressure case). The reddish lines are the trajectories calculated with the BE model for crack propagation [Maccaferri *et al.*, 2011] for various dimensionless magma overpressure ( $P_m/P_{\text{load}} = 0.25, 0.5, 0.6, 0.75, 1, 1.5$ , and  $2$ ). (b) Normalized normal stress seen by the dike along its trajectory ( $\sigma_c/P_{\text{load}}$ ) as a function of elevation. The plain and dashed lines are, respectively, for the dike following  $\sigma_1$  (small driving pressure case with  $\sigma_{c-\text{sdp}} = \sigma_3$ ) and for the vertically ascending dike (large driving pressure case with  $\sigma_{c-\text{idp}} = \sigma_{xx}$ ). The red dash-dotted line is for the trajectory obtained when  $P_m/P_{\text{load}} = 0.75$ .

grid length. We use a time step small enough to ensure that the front is not advancing at each time step. Convergence is checked by comparing runs with different space and time steps. We also check that mass conservation is satisfied on the scale of the whole dike, using the instantaneous volume change and the basal flux issued from the numerical computation.

Each part of this model could be made more complex by integrating heterogeneous properties within the crust (density layering effect as in Taisne and Jaupart [2009] and Traversa *et al.* [2010]) or evolution of magma properties, for instance, as induced by gas exsolution [Taisne and Jaupart, 2011]. Moreover, the model could be applied to horizontally propagating dikes by substituting the pressure gradient due to buoyancy with a lateral pressure gradient associated to tectonic stresses or volcano load [Pinel and Jaupart, 2004; Maccaferri *et al.*, 2016].

### 3. General Results

#### 3.1. Surface Load: Edifice Construction

We assume a configuration as in Watanabe *et al.* [2002, Figure 5b] in order to compare our calculations with those experiments. We consider a uniform load applied on the surface over a segment of half-width  $L_{\text{load}}$ . A deviatoric stress field is generated with a maximum compression in the vertical direction beneath the load (Figure 2a) of intensity proportional to  $P_{\text{load}}$ . The depth to which this compressive stress field extends is controlled by  $L_{\text{load}}$ .

We initiate dikes at a dimensionless offset from the center of the load  $X_{in}^* = 2.8$  and a dimensionless depth  $Z_{in}^* = 2.7$  for a range of values of  $N_2 = P_m/P_{\text{load}}$ . Similar to what is described by Watanabe *et al.* [2002], the dikes

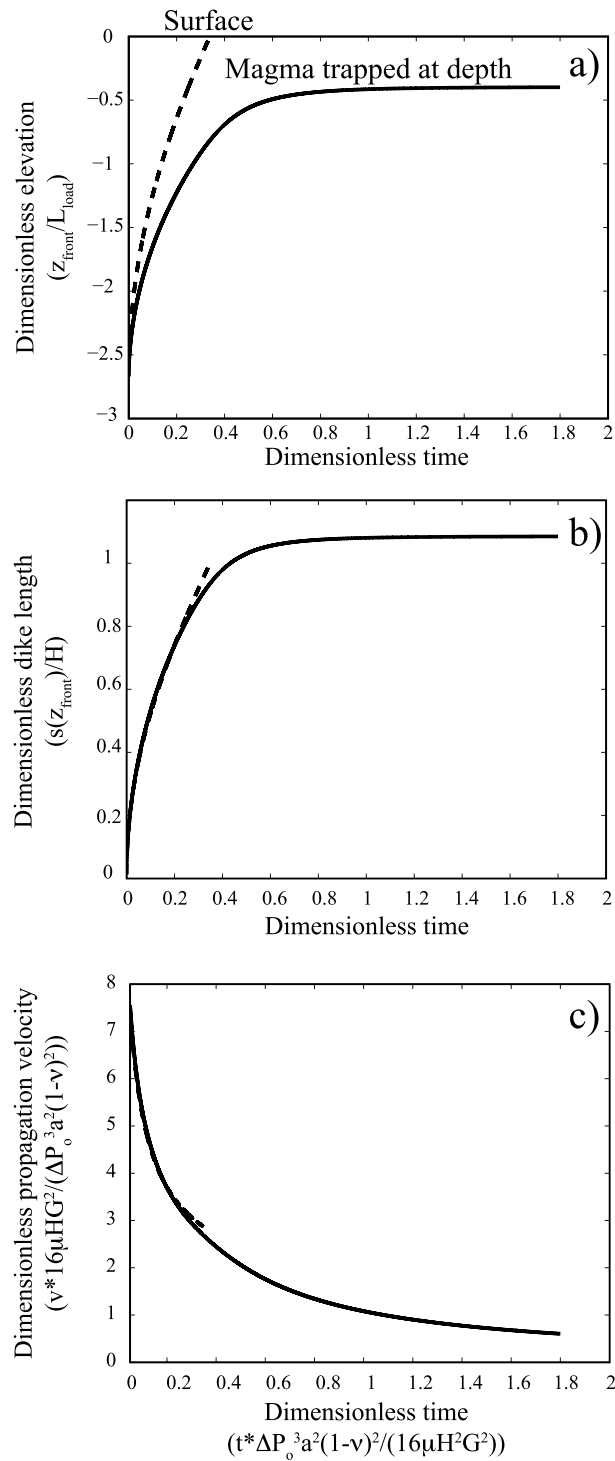


**Figure 3.** Front position as a function of time for the two end-member cases (ldp and sdp cases) trajectories when a load (of half-length  $L_{\text{load}}$  and amplitude  $P_{\text{load}}$ ) is applied at the surface. (a) Front elevation normalized by the load size as a function of time. (b) Dike length as a function of time. (c) Velocity as a function of time. Plain and dashed lines are, respectively, for the deflected (sdp case,  $N_1 = 0, N_2 = 0.25$ ) and vertical ascent (ldp case,  $N_1 = 0, N_2 = 2$ ). Dimensionless parameters are represented. For the vertical ascent, the calculation is arrested when the dike reaches the surface, whereas for the deflected trajectory the calculation is arrested after a given amount of iterations. Note that the length scale is the same in both cases; however, when considering the same load applied, as the magma overpressure,  $\Delta P_o$ , at the dike bottom is 8 times larger for the vertical ascent, the time scale (see equation (5)) is different (512 times smaller for the large driving pressure case (vertical ascent), such that the propagation is much quicker).

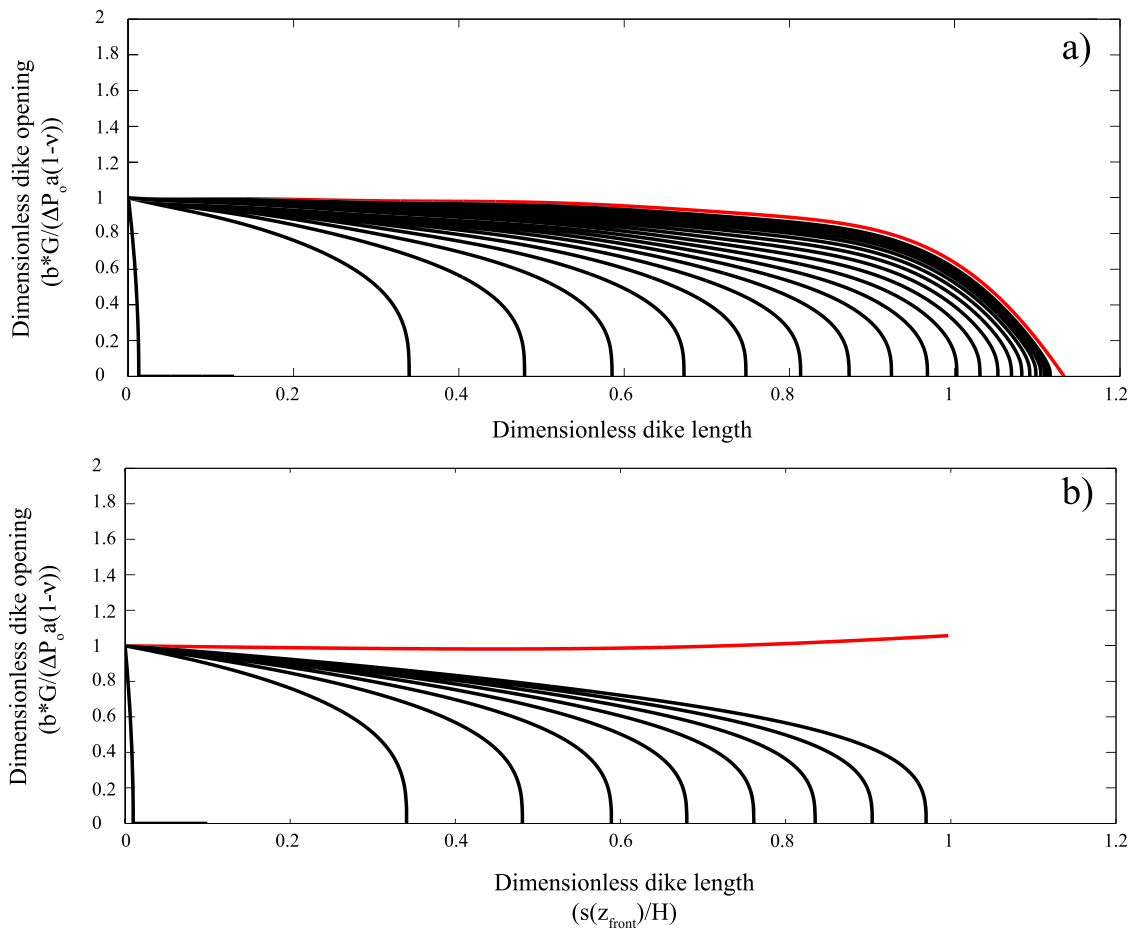


**Figure 4.** Dike opening as a function of time for the two end-member cases (ldp and sdp cases) trajectories when a load (of half-length  $L_{\text{load}}$  and amplitude  $P_{\text{load}}$ ) is applied at the surface and when there is no density contrast between the magma and the surrounding rocks (the magma driving pressure only comes from the bottom reservoir overpressure). The dimensionless dike width is represented as a function of the dimensionless dike length, along the trajectory in the initial stage, and at a regular dimensionless time step of 0.04. The red line is for the opening of a static dike (obtained by combining equations (2) and (1) with  $p = 0$ ). (a) Deflected trajectory (sdp case,  $N_1 = 0$ ,  $N_2 = 0.25$ ). (b) Vertical trajectory (ldp case,  $N_1 = 0$ ,  $N_2 = 2$ ). Note that the vertical length scale is the same in both cases; however, as the magma overpressure,  $\Delta P_o$ , at the dike bottom is larger for the vertical ascent, the scale for the half-width (see equation (6)) is different (8 times larger for the vertical ascent); the time scale (see equation 5) is also different (512 times smaller for the vertical ascent) such that the propagation is much quicker and the dike much thicker in the case of vertical ascent (for  $N_2 = 2$ ).

become all the more deflected as the magma driving pressure is small compared to the load. The two end-member dike trajectories, represented as black dashed (ldp case) and plain lines (sdp case), respectively, in Figure 2a, intersect the surface at a normalized distance of  $\approx 2$  from each other.

The normal stress field  $\sigma_c$  acting on the dike wall (represented on Figure 2b for the two end-member cases and for  $N_2 = 0.75$ ) varies significantly along each trajectory. In particular, for both the ldp and the mdp cases,  $\sigma_c$  decreases while the dike rises (Figure 2b). On the contrary, for the sdp case, the rising magma becomes deflected toward the load and enters a region of strong compression (higher  $\sigma_c$ ). Note that even if all trajectories share the same starting point, the initial value of  $\sigma_c$  may differ due to different crack orientations.  $\sigma_c$  is minimum for cracks aligned to  $\sigma_1$ .

The dyke trajectory defines the functions  $z(s)$  and  $\sigma_c(s)$  which are interpolated using a polynomial function, and their first two derivatives are used as input for the dynamical calculation (equation (7)). The bottom boundary condition is taken such that  $b(s = 0) = 1$ , equivalent to taking the magma overpressure at the bottom of the dike equal to the magmatic reservoir overpressure  $\Delta P_o$ , when  $\Delta P_o$  is defined as an overpressure with regard to the local surrounding pressure (lithostatic plus local stress field). This is consistent with the fact that a magma overpressure is required with regard to  $\sigma_c$  to initiate fracturing the rock. Note that the

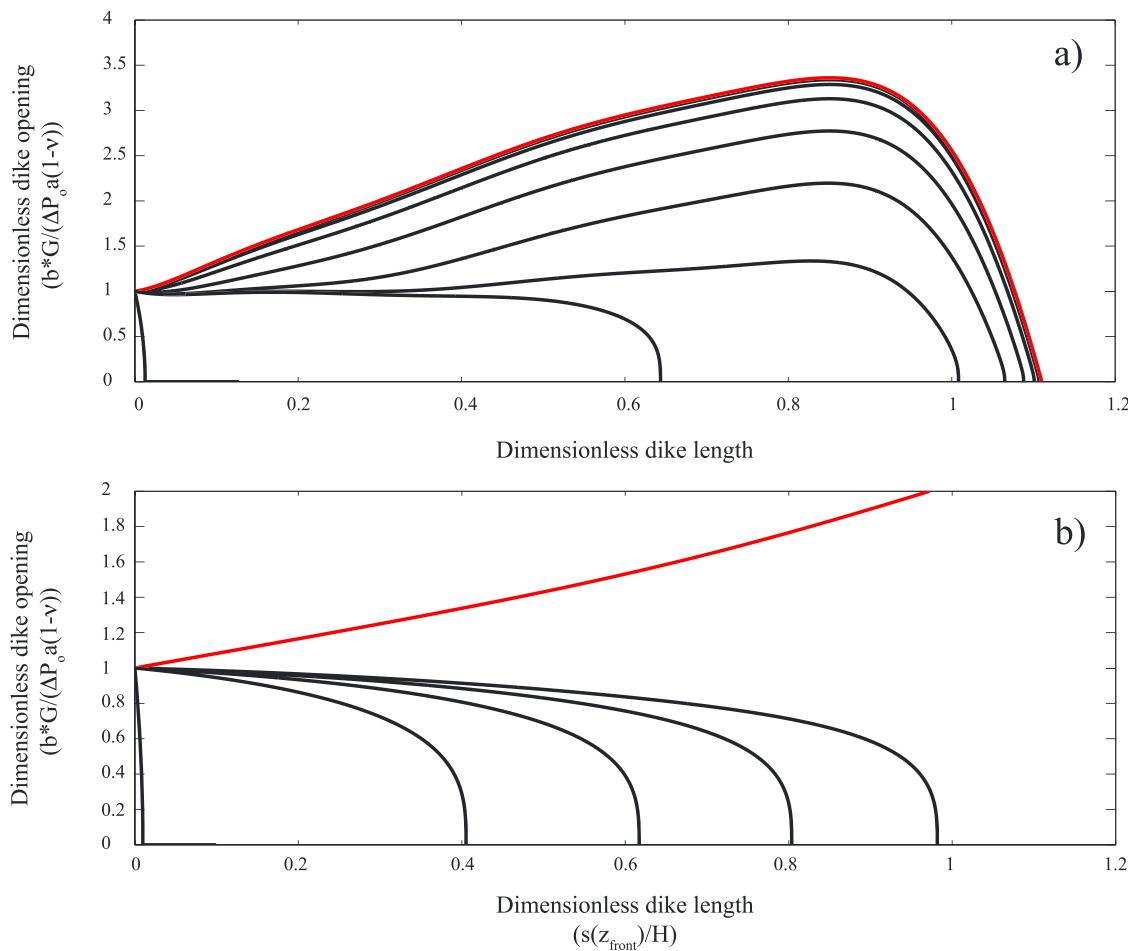


**Figure 5.** Dike opening as a function of time for the two end-member cases (ldp and sdp cases) trajectories when a load (of half-length  $L_{\text{load}}$  and amplitude  $P_{\text{load}}$ ) is applied at the surface and when buoyancy is acting. The dimensionless dike width is represented as a function of the dimensionless dike length, along the trajectory in the initial stage, and at a regular dimensionless time step of 0.04. The red line is for the opening of a static dike (obtained by combining equations (2) and (1) with  $p = 0$ ). (a) Deflected trajectory (sdp case,  $N_1 = 5$ ,  $N_2 = 0.25$ ). (b) Vertical trajectory (ldp case,  $N_1 = 0.9$ ,  $N_2 = 2$ ). Note that the vertical length scale is the same in both cases; however, as the magma overpressure,  $\Delta P_o$ , at the dike bottom is larger for the vertical ascent, the scale for the half-width is different (see equation (6)) (25 times larger for the vertical ascent); the time scale (see equation (5)) is also different (16,000 times smaller for the vertical ascent) such that the propagation is much quicker and the dike much thicker in the case of vertical ascent (for  $N_2 = 2$ ).

propagation velocity will not be sensitive to the absolute value of the confining stress at the starting position, but it will depend on the confining stress gradient along the trajectory.

With a large driving pressure ( $N_2 = 2$ ) the magma reaches the surface (dashed line in Figure 3), while it gets trapped at a depth  $\approx 0.5L_{\text{load}}$  for a low driving pressure ( $N_2 = 0.25$ , plain line in Figure 3). In the latter case the dyke is deflected toward the compressive stress induced by the load and its progression is inhibited, its lengths stop increasing (Figure 3b), and its velocity tends to zero (Figure 3c). These results are obtained with the magma driving pressure equal to the reservoir overpressure ( $\rho_c = \rho_m$  or  $N_1 = 0$ ), but similar results are obtained for buoyant magma ( $N_1 > 0$ ). Both for large ( $N_2 = 2$ ) and small ( $N_2 = 0.25$ ) magma driving pressure, dikes decelerate during propagation; however the velocity is higher for the ldp case (Figure 3c).

When the dike velocity decreases, the dike thickens. This is shown in Figure 4a, where the propagating tip of the dike stops before reaching the surface, the dike opening profiles (normalized value) get thicker (particularly in its upper part) than the ones computed for the large driving pressure case (Figure 4b) where the velocity decrease is much smaller. If the dike stops, it reaches the static overpressure profile, with the viscous pressure drop equal to zero. This behavior occurs whatever the buoyancy considered (for any parameter  $N_1$ ); however, different values of  $N_1$  affect the final shape of the dike. With buoyant magma ( $N_1 > 0$ ) the overpressure increases with vertical dike growth, and the final dike thickness (static profiles in Figure 5) increases

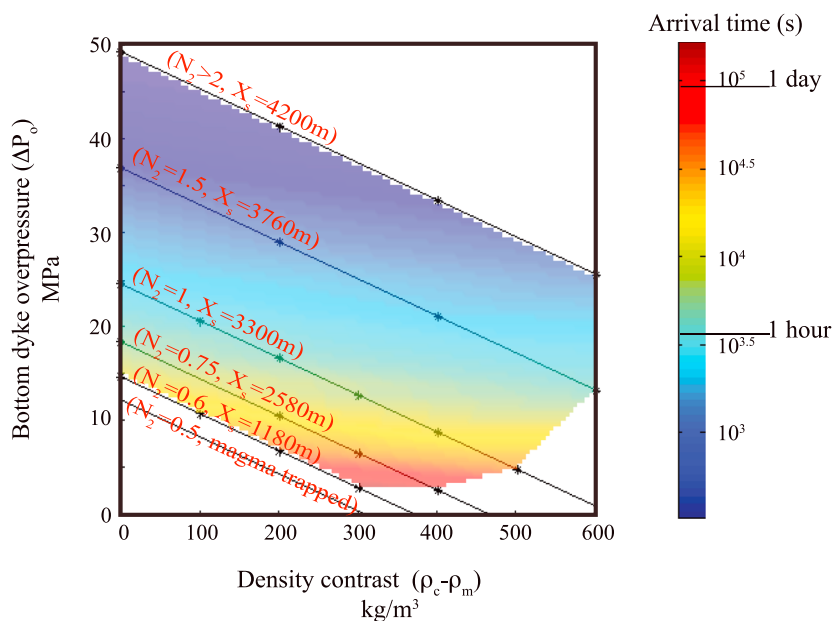


**Figure 6.** Duration of the dike propagation as a function of the dike bottom overpressure ( $\Delta P_0$ ) and the density contrast between the rock and the magma ( $\rho_c - \rho_m$ ). The calculation is performed for a specific set of parameters: the applied load is defined by  $P_{\text{load}} = 24.525$  MPa (corresponding to the weight of a column of 1 km of rocks) and  $L_{\text{load}} = 1.5$  km, the starting depth is  $H = 4$  km, the starting lateral distance from the center of the load is  $x_{\text{off}} = 4.2$  km, the rock density is  $\rho_c = 2500$  kg m $^{-3}$ , the crust is characterized by its elastic parameters  $v = 0.25$  and  $G = 1.125$  GPa, and the magma viscosity is set to  $\mu = 2000$  Pa.s. The dike half-breadth is set to 100 m. Arrival times represented by the range of colors are extrapolated from the numerical simulations performed and marked as stars. Each line corresponds to a given value of  $N_2$ , which means a given magma path. The distance from the center of load at which the dike reaches the surface,  $X_s$ , is also reported.

along the dike profile from the reservoir to the region of high compression where the dike stops (Figure 5a). The dike thickening associated with the velocity decrease had already been evidenced for a dike rising vertically beneath a load [Pinel and Jaupart, 2000] or across a lithological discontinuity [Taisne and Jaupart, 2009; Traversa et al., 2010].

Calculations for a range of intermediate magma driving pressures  $0.25 < N_2 < 2$  show that the propagation lasts longer for a lower magma driving pressure (Figure 6). When the magma driving pressure is too small (here for  $N_2 < 0.6$ ), the magma never reaches the surface and gets trapped at depth. Also, when the magma pressure decreases, the amount of deflection increases and the magma reaches the surface closer to the center of the load (Figure 6).

To summarize, our modeling scheme reproduces the effect of surface loading on the propagation path and velocity of a dike in agreement with previous experimental results. Our model retrieves correctly the result that a load applied at the surface tends both to deflect and to slow down ascending dikes initially offset from the center of the load, the effect being larger when the applied load is larger with regard to the magma driving pressure. As also shown by Watanabe et al. [2002], the amount of deflection depends on the starting position of the dike. A dike rising beneath the load center will not be deflected whatever its overpressure. However, when entering the compressive stress field induced by the load, it will slow down, with a larger deceleration for smaller  $N_2$ .

### 3.2. Surface Unloading: Caldera Formation

Next, we apply the model to a case of unloading. Unloading events may be modeled with tractions applied to the surface (negative  $P_{\text{load}}$ ). Rifts are characterized by horizontal extension; thus, following Maccaferri et al. [2014], we apply a horizontal tensile stress  $P_{\text{load}}/10$ . This ensures that  $\sigma_1$  is oriented vertically in the far field, thus favoring eruption. As already evidenced by Maccaferri et al. [2014] and Corbi et al. [2015], surface unloading induces a deviatoric stress field beneath the unloaded region with  $\sigma_3$  oriented vertically, thus favoring the formation of sills. A dike rising vertically beneath the negative load will be deflected outward all the more when its overpressure is small with regard to the amplitude of the traction applied (Figure 7).

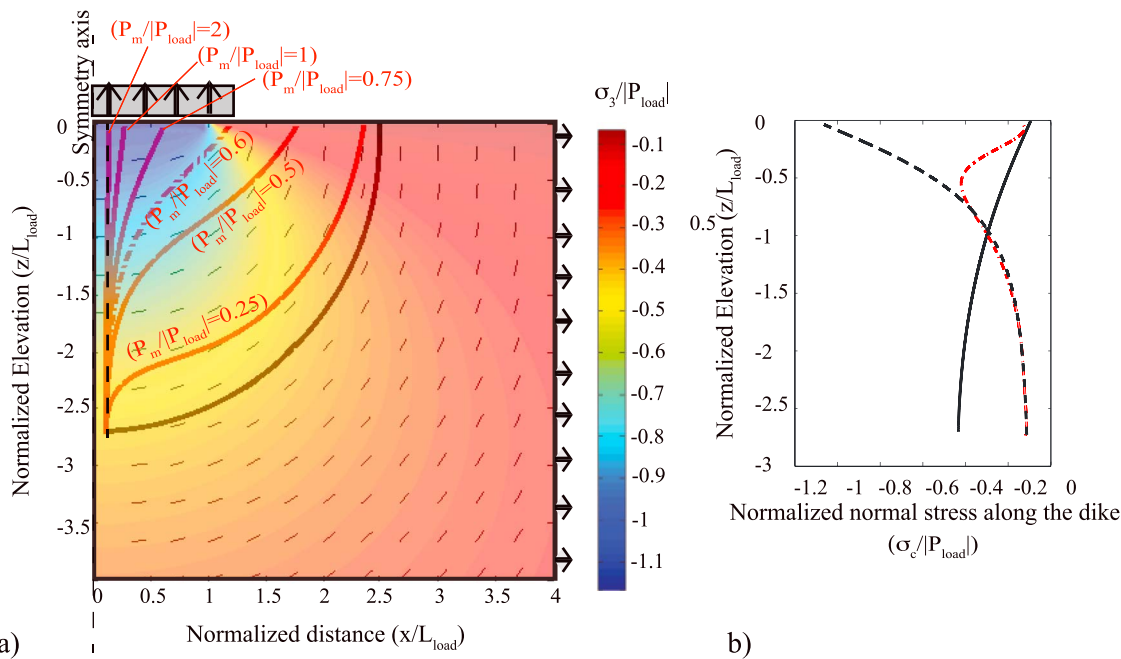


**Figure 7.** Dike trajectories in a crust unloaded at the surface and characterized by a homogeneous extension along the horizontal axis. (a) Stress induced by an unloading of amplitude  $|P_{load}|$  is applied at the surface over a segment  $2L_{load}$  of a homogeneous elastic medium together with a homogeneous extension of amplitude  $0.1|P_{load}|$ . Black lines are for the orientation of  $\sigma_1$ . The color scale is for the amplitude of  $\sigma_3$ . The plain line is the path of a dike starting at normalized distance depth 2.7 almost below the load (at a lateral dimensionless distance of 0.1) and following  $\sigma_1$  (small driving pressure case); the dashed line is the path of a vertical dike (large driving pressure case). The reddish lines are the trajectories calculated with the BE model for crack propagation [Maccaferri et al., 2011] for various dimensionless magma overpressure ( $P_m/|P_{load}|=0.25, 0.5, 0.6, 0.75, 1$ , and  $2$ ). (b) Normalized normal stress seen by the dike along its trajectory ( $\sigma_c/|L_{load}|$ ) as a function of elevation. The plain and dashed lines are, respectively, for the dike following  $\sigma_1$  (small driving pressure case with  $\sigma_{c-sdp}=\sigma_3$ ) and for the vertically ascending dike (large driving pressure case with  $\sigma_{c-ldp}=\sigma_{xx}$ ). The red dash-dotted line is for the trajectory obtained when  $P_m/|P_{load}|=0.6$ .

Since  $\sigma_1$  is horizontal at the starting position of the dikes, whatever the magma driving pressure considered, the dikes take some time to reorient horizontally. The distance required for the dike to follow  $\sigma_1$  increases with the magma driving pressure. This result is consistent with experimental results [Menand et al., 2010].  $\sigma_c$  increases toward the surface for a deflected dike, thus inhibiting propagation, whereas it decreases toward the surface for a vertical dike, thus favoring propagation (Figure 7b). The main difference to the loading case is that, as vertical dikes here ascend beneath a negative load, the variations of  $\sigma_c$  along its trajectory are larger than for the loading case. Here we start the dikes with a small offset  $x_{off}/L_{load}=0.1$  so that  $\sigma_c$  along the deflected trajectory starts to increase at greater depth and is more progressive than for the loading case. For the intermediate case ( $N_2=0.6$ ), the confining stress first decreases, along the vertical part of the trajectory, and then starts to increase at a depth  $\approx L_{load}/2$ , reaching the same value as for the deflected dike at the surface.

The deflected intrusion decelerates strongly because  $\sigma_c$  increases along a trajectory that diverges away from the tensile stress field induced by the unloading (Figure 8). A dike characterized by a small magma driving pressure gets trapped at depth. As in the previous case, the velocity decrease induced by the increase of  $\sigma_c$  is associated with a thickening of the intrusion (see Figure 9a). When the magma is trapped at depth, its shape is controlled by the static pressure profile (Figure 9a).

To summarize, a dike rising vertically beneath a rift or a caldera is deflected outside the topographic depression and its velocity is much lower than it would have been if it had risen vertically. This deflection together with the velocity decrease is consistent with experimental results obtained for a caldera context [Corbi et al., 2016].

#### 4. Case Study: The July 2001 Etna Eruption

##### 4.1. Summary of the Eruptive Event

A large flank eruption occurred in July 2001 at Mount Etna, ending an intense seismic swarm that had lasted for more than 4 days and was located at shallow depth (above 3 km below sea level) beneath the summit

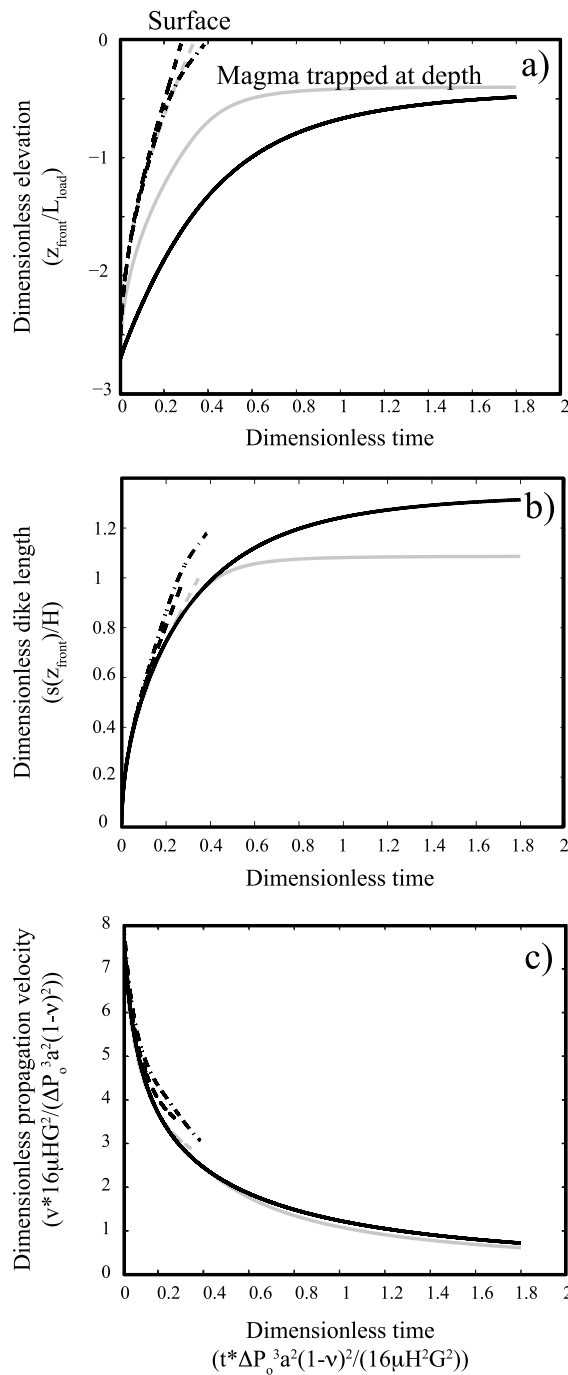


**Figure 8.** Front position as a function of time when an unloading (of half-length  $L_{\text{load}}$  and amplitude  $|P_{\text{load}}|$ ) is applied at the surface together with a homogeneous horizontal extension of amplitude  $0.1 * |P_{\text{load}}|$ . (a) Front elevation normalized by the load size as a function of time. (b) Dike length as a function of time. (c) Velocity as a function of time. Plain and dashed lines are, respectively, for the deflected (sdp case,  $N_1 = 0, N_2 = 0.25$ ) and vertical ascent (ldp case,  $N_1 = 0, N_2 = 2$ ). The dash-dotted line is for the intermediate case with  $N_1 = 0$  and  $N_2 = 0.6$ . Dimensionless parameters are represented. For the vertical ascent as well as the case with  $N_2 = 0.6$  the calculation is arrested when the dike reaches the surface, whereas for the deflected trajectory the calculation is arrested after a given amount of iterations. Note that the length scale is the same in both cases; however, when considering the same load applied, as the magma overpressure,  $\Delta P_o$ , at the dike bottom is, respectively, 2.4 and 8 times larger for, respectively, the case with  $N_2 = 0.6$  and the vertical ascent compared to the small driving pressure case, the time scale (see equation (5)) is different (respectively 13.8 and 512 times smaller for, respectively, the intermediate case and the large driving pressure case (vertical ascent), such that the propagation is quicker). Previous results obtained for the loading case (Figure 3) are reported in grey for comparison.

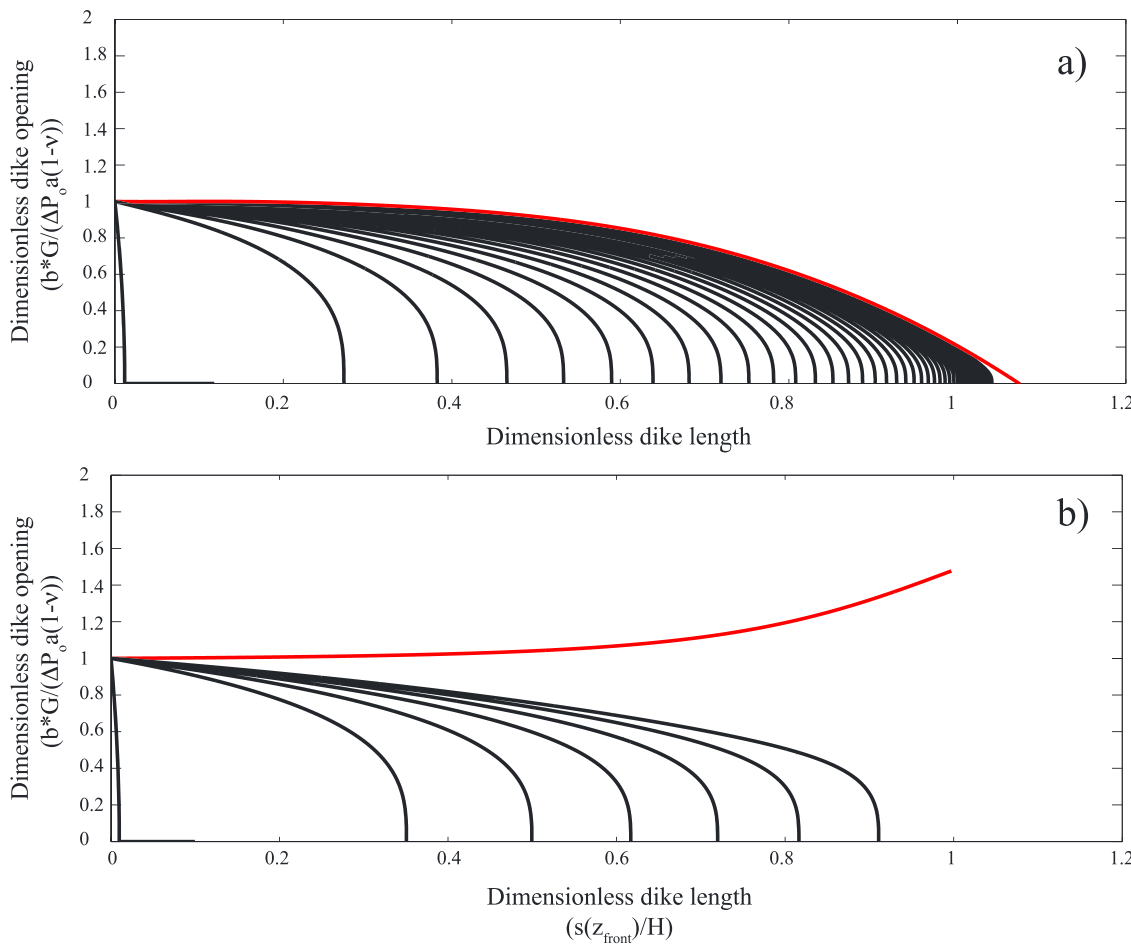


**Figure 9.** Dike opening as a function of time for the two end-member cases (ldp and sdp cases) trajectories when an unloading (of radius  $R_{\text{load}}$  and amplitude  $|P_{\text{load}}|$ ) is applied at the surface together with a homogeneous horizontal extension of amplitude  $0.1 * |P_{\text{load}}|$  and when there is no density contrast between the magma and the surrounding rocks (the magma driving pressure only comes from the bottom reservoir overpressure). The dimensionless dike width is represented as a function of the dimensionless dike length, along the trajectory in the initial stage, and at a regular dimensionless time step of 0.04. The red line is for the opening of a static dike (obtained combining equations (2) and (1) with  $p = 0$ ). (a) Deflected trajectory (sdp case,  $N_1 = 0$ ,  $N_2 = 0.25$ ). (b) Vertical trajectory (ldp case,  $N_1 = 0$ ,  $N_2 = 2$ ). Note that the vertical length scale is the same in both cases; however, as the magma overpressure,  $\Delta P_o$ , at the dike bottom is larger for the vertical ascent, the scale for the half-width (see equation (6)) is different (8 times larger for the vertical ascent); the time scale (see equation 5) is also different (512 times smaller for the vertical ascent) such that the propagation is much quicker and the dike much thicker in the case of vertical ascent (for  $N_2 = 2$ ).

area [Patane et al., 2002]. The 2001 eruption lasted for 3 weeks and was the first lateral eruption since the large 1991–1993 event. The 2001 eruption was unusual as it involved two different magma sources following different pathways [Métrich et al., 2004]. The first fissure opened on 17 July at 2700 m (above sea level), fed by a lateral propagation from the central conduit. The consecutive vents, which opened on 18 and 19 July at 2100 m and 2550 m above sea level, respectively, were fed by an eccentric dike rising vertically [Métrich et al., 2004; Bonforte et al., 2009]. The position of the vertical dike (which reached the surface on 18 July) has been inferred based on seismic deformation as well as magnetic data around 1.4 km east of the eruptive vent [Patane et al., 2002; Bonaccorso et al., 2002; Del Negro and Currenti, 2003; Martinez-Arévalo et al., 2005]. The magma migrated below the surface for 1 or 2 days before erupting, and the last part of its path was clearly inclined toward the west [Del Negro and Currenti, 2003; Bonforte et al., 2009]. The final stage of the dike propagation in the last 1–2 km below the surface and the 2 days before it reached the surface was marked by a clear velocity decrease as well as a deflection toward the west [Bonaccorso et al., 2010]. Based on the analog experiments of Watanabe et al. [2002], Bonaccorso et al. [2010] interpreted the final deflection of the dike as due to the local load formed by the volcanic pile westward of Valle del Bove and inferred an overpressure

**Table 1.** Parameters Used for the Etna July 2001 Eruption

	Parameter	Value
Dike starting lateral distance	$X$	2.4 km
Dike starting depth	$H$	3.1 km
Dike half-breadth	$a$	100 m
Load radius	$L_{\text{load}}$	1.5 km
Load pressure	$P_{\text{load}}$	12.26 MPa
Crustal rigidity	$G$	1.125 GPa
Poisson's ratio	$\nu$	0.25

within the dike between 4 and 9 MPa. In the following, we estimate the dike bottom overpressure based on the duration of the dike propagation and on the fact that it took 2 days for the magma to reach the surface once it started to deflect.

#### 4.2. Estimation of the Magma Overpressure

We consider the stress field induced by a load of radius 1.5 km and height 500 m to account for the topography of Etna's summit area acting above the ascending dike. Based on geodetic measurements [Bonaccorso *et al.*, 2002], we assume a dike starting depth of 3100 m below the applied load. As a strong dike deflection was observed, we assume a low overpressure dike (trajectory follows closely  $\sigma_1$ ) and derive the starting offset by ensuring that it is consistent with a final lateral deflection of the dike of 1.4 km. The initial offset from the center of the load is thus set at 2.4 km. Dynamical calculations along the trajectory are performed for various magma overpressure  $\Delta P_o$  and crustal densities thus varying  $N_1$  and  $N_2$ . Other parameters are listed in Table 1. Note that the half-breadth  $a$  has been taken to 100 m, which is 1 order of magnitude smaller than the value estimated from geodetic data [Bonaccorso *et al.*, 2010]. This is necessary in order to fulfill the condition  $a \ll H$  required by our dynamical model. However, in order to have a consistent time scale, we accordingly lowered the value of the crustal rigidity by a factor of 10 [Bonaccorso *et al.*, 2010]. The boundary condition applied at the dike bottom is here  $b(s = 0) = 1 - \sigma_c(s = 0)/P_{\text{load}}$ . This means that the reservoir overpressure  $\Delta P_o$  is here defined as the magma excess pressure with regard to the lithostatic pressure, which makes it easier to interpret. We assume a range of magma viscosity values and evaluate the results' consistency with a propagation of 2 days for various values of magma overpressure and magma-rock density contrast (Figure 10). When the magma driving pressure (magma bottom overpressure plus buoyancy) increases, dike propagation

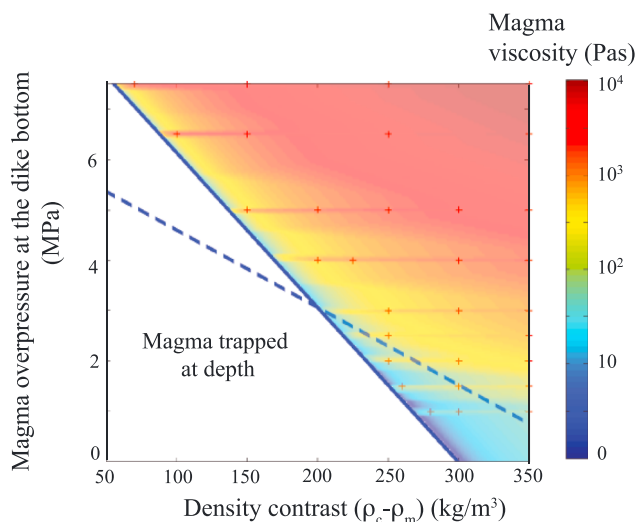


**Figure 10.** Magma viscosity consistent with magma propagation along the deflected path (following  $\sigma_1$ ) within 2 days. Parameters used are listed in Table 1. Red crosses are for the numerical simulations performed. The plain line is the threshold overpressure for magma to reach the surface. The dashed line is the threshold magma overpressure for having a deflected dike (below this line the dike path can be considered to follow  $\sigma_1$ ). This limit is obtained considering that  $N_2 = 0.5$  but with a length scale of  $H/2$  for the buoyancy estimation.

is quicker so that a larger viscosity is required in order to obtain a 2 day long propagation. The magma rising in the eccentric dike has been characterized as a volatile-rich primitive basalt with a high dissolved content of water (3.4 wt %) [Métrich *et al.*, 2004], whose viscosity at erupting temperature is expected to be below 100 Pa.s [Giordano and Dingwell, 2003]. Based on our results (Figure 10), an upper bound for  $\mu = 100$  Pa.s corresponds to  $\Delta P_o < 4$  MPa. This value is close to the value of 4–8 MPa derived by Bonaccorso *et al.* [2010] based on the magma pathway.

We can now check a posteriori whether for the 2001 Etna eruption the magma driving pressure was small, consistent with our initial assumption. The dashed line represented on Figure 10 is the threshold of low magma overpressure (below this line the dike pathway follows  $\sigma_1$ ). This limit is obtained considering  $N_2 = 0.5$  and using a length scale equal to half the initial depth ( $H/2$ ) in order to avoid an overestimation of the buoyancy effect, such that the limit is given by  $\Delta P_o = 0.5(1 - gH(\rho_c - \rho_m))$ .

## 5. Discussion

### 5.1. Trajectory Estimation for Intermediate Cases

Our two-step approach has to be considered as a first attempt to solve for both dike trajectory and velocity. The approach has the advantage that it is relatively simple, and it can be applied quickly, provided that the stress field can be approximated as 2-D (i.e., the stress field does not significantly change toward the out-of-plane direction, along a distance of the order of the dike's half-breadth). With the Etna 2001 eruption study we prove that incorporating into models information on the propagation velocity provides additional constraints on the physical properties of an intrusion. However, we make use of quite drastic simplifications that we are now discussing in detail.

We use in successive steps two separate models that rely on slightly different assumptions. Whereas in the fracturing-dominated regime used in Step 1 the force controlling the dike shape and counterbalancing the buoyancy is the fracture toughness, in the lubrication dynamic model used in Step 2 this force is the viscous pressure drop. One of the direct consequences is that the crack of Step 1 has a finite length and no tail, such that it is not linked to any magma reservoir. Consequently, the propagation in Step 1 is independent from the magma reservoir overpressure, whereas in Step 2 the dike is connected to a magma source that contributes to its driving force. In the following we discuss the trajectories provided by Step 1 for intermediate cases based on previous experimental results. Then, we briefly discuss the potential influence of viscosity on the magma path and finally discuss in depth the meaning of the magma driving pressure.

#### 5.1.1. Magma Path: Comparison of Experimental and Numerical Results

The numerical model used to calculate the dike trajectories neglects the viscous pressure drop induced by the fluid flow. This approach well describes the force balance within the crack nose [Lister, 1990a], it is suitable for low viscosity fluids and mimics the conditions of experiments with air-filled cracks propagating in gelatin. Our simulated dike trajectories overlap with experimental trajectories, however, corresponding to slightly smaller magma driving pressure [Watanabe *et al.*, 2002]. For instance, in our case a larger value of  $N_2$  (around 2 compared to 0.68 for experimental results) is required to observe a vertical propagation.

An important factor that can explain the small discrepancy is that the stress field within the gelatin for the experimental setup used by Watanabe *et al.* [2002] does not correspond exactly to a uniform load applied to a half-space as modeled by the analytical solutions (see Figure 11 where the normalized shear stress  $\sigma_{xz}/P_{load}$  for the analytical solutions is compared to a numerical calculation for the gelatin box used by Watanabe *et al.* [2002]). The calculation was done in 3-D with the commercial software COMSOL applying a zero displacement condition at the lateral and bottom boundaries of the gelatin). The comparison shows that the rigid box wall reduces by a factor of 2 the shear stress induced within the gelatin by the load at the starting position of the crack. The shear stress has a strong influence on the crack deflection [Lawn and Wilshaw, 1975; Watanabe *et al.*, 2002]. It follows that within the analog experiments the load effect is underestimated, thus requiring larger loads for dike deflection. The rigid walls of the experimental setup may also modify the stress perturbation induced by the crack itself. However, the stress perturbation induced by the crack around its tip is expected to be localized at a distance smaller than three times the crack half-length [Daniels and Menand, 2015], such that this last effect may be neglected here. The discrepancy between the numerical and experimental results may be also due to 3-D effects that are not considered in the numerical simulations. Moreover, the dike trajectory, for a given dike overpressure, also depends on the initial crack length. The crack length normalized by the load half-width in the experiments varied from 1.66 to 2.1, whereas in our calculation it varies from 1 for  $N_2 = 0.25$  to 7 for  $N_2 = 2$ . For cases where  $L_z/L_{load}$  is similar in experimental and numerical cases (for  $0.18 < N_2 < 0.6$ ),

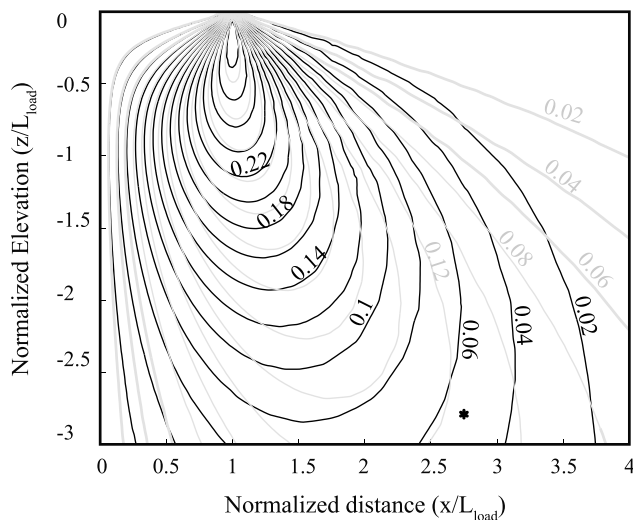


**Figure 11.** Contour lines of the shear stress  $\sigma_{xz}$  normalized by the applied load (contour line distance is set to 0.02). Black and grey curves are, respectively, for the experimental setup used by Watanabe *et al.* [2002] (calculated using COMSOL commercial software) and for an elastic half-space (analytical formulation from Watanabe *et al.* [2002]). The star is for the starting position of the dike as considered in section 3.1 and in Figure 5b of Watanabe *et al.* [2002].

the magma driving pressure required to follow the same trajectory is always smaller in experimental results, such that the influence of the initial crack length is not expected to be responsible for a systematic difference between our numerical simulations and gelatin experiments by Watanabe *et al.* [2002].

### 5.1.2. Magma Path: Influence of the Viscosity

The discrepancies discussed above are quite small. The numerical calculation agrees fairly well with analog results, and we conclude that the first step of our model provides reliable trajectory estimates for low viscosity magmas. However, the main intrinsic limitation of our two-step model is that it precludes any influence of the dynamics of the magma flow on the dike trajectory. Numerical models for magma dynamic propagation in 1-D have shown that magma viscosity or flow rate influences both dike velocity and shape [Pinel and Jaupart, 2004]. It is thus expected that a change of magma viscosity may also influence the magma pathway. A proper solution to this problem may require integration of the models at each numerical step, in order to solve simultaneously for the direction of propagation and flow conditions.

### 5.1.3. How to Consistently Define the Magma Driving Pressure?

In Step 1, dike trajectories are here computed excluding a connection to a magma source, thus focusing on the dike nose description, where viscous force can be neglected [Lister, 1990a]. In such a case the dike driving pressure (the overpressure at the upper tip of the dike) is given by the magma buoyancy, which depends on the vertical elongation of the dike and thus on the dike dip angle. However, our simulations show that the overpressure due to buoyancy remains of the same order of magnitude during propagation (with the dike length increasing when the dip angle decreases), so that the ratio between the magma driving pressure and the load applied at the surface remains approximately constant, at least in the cases we considered here.

When computing velocities, we consider a dike linked to a feeding reservoir by an open tail. The magma driving pressure is the sum of the magma overpressure within the reservoir and the overpressure due to magma buoyancy integrated over the whole vertical extension of the dike. In realistic cases, the reservoir overpressure decreases as a result of magma loss into the growing intrusion [Buck *et al.*, 2006; Rivalta, 2010]. This effect may be small as long as the magma reservoir is large with regard to the volume of the intrusion or as long as the magma is highly compressible [Traversa *et al.*, 2010]. In these cases the magma overpressure at the bottom may be considered constant during dike propagation. Therefore, if the buoyancy contribution is negligible (small  $N_1$ ), the dike driving pressure will be constant during propagation, similar to what is obtained with the numerical model used to compute the dike trajectories. Finally, for small  $N_1$ , the evolution of the driving pressure during the propagation is the same for both models, and therefore, we can consistently use the output of the first model (trajectory calculation) as input for the second one (velocity calculation). However, if we use

$N_1 > 0$ , corresponding to a largely buoyant magma, to compute the dike velocity, the driving pressure due to magma buoyancy will considerably increase when the dike rises toward the surface and will be maximum (equal to  $(\rho_c - \rho_m)gH$ ) when the dike extends all the way from the reservoir to the surface. As a consequence, the ratio between the magma driving pressure and the load applied at the surface increases when the dike propagates toward the surface. This ratio is maximum and equal to the dimensionless parameter  $N_2$  when the dike reaches the surface. This would lead to an inconsistency: the velocity along the dike trajectory is computed in Step 2 at first (when the dike starts propagating) using a magma driving pressure smaller with respect to the one used to compute the dike path in Step 1. Later, when the dike is well developed, the magma driving pressure increases and reaches the value considered for the dike trajectory calculation. The trajectory calculated such tends to underestimate the deflection. Nevertheless, even in such case the trajectory derived using the BE model represents a reasonable first-order approximation for the expected trajectory when either  $N_1$  or  $N_2$  are small. Moreover, it is consistent with the dike nose behavior reflecting the effect of the local buoyancy and stress gradient [Lister, 1990a; Taisne and Jaupart, 2009].

### 5.2. Magma Pressure Estimations

In this study, we estimated the magma bottom overpressure at 3 km depth to be less than 4 MPa based on the dike velocity inferred from geophysical observations for the 2001 flank eruption at Etna. Studying the same event and using the same data set, but interpreting the deflection of magma trajectories based on Watanabe et al. [2002], Bonaccorso et al. [2010] inferred an overpressure within the dike around 4–8 MPa at the same depth. They extrapolated this value to a reservoir overpressure of 7–15 MPa around 5 km below sea level. Other studies have previously used the geophysical signal record during a magma propagation event to derive a reservoir overpressure. Einarsson and Brändsdóttir [1980] used an analytical model in order to interpret the velocity of a lateral dike propagating away from Krafla Volcano in July 1978. They inferred the dike tip position from seismic epicenters and derived a reservoir overpressure around 1 to 4 MPa at 2–3 km depth. Traversa et al. [2010] used a dynamical model to derive the reservoir overpressure at Piton de la Fournaise to be less than 2.2 MPa at 2–3 km depth based on the constant seismic rate recorded preceding the August 2003 eruption. All these studies took advantage of geophysical signals recorded during magma propagation at depth to estimate a reservoir overpressure. Contrary to estimates based on deformation signals, no assumption has to be made on the Young modulus characterizing the crust. All these reservoir overpressure values fall within the range of expected values for rock tensile strength [Haimson and Rummel, 1982; Benson et al., 2012] and are consistent with a rupture criterion at the chamber wall, such that the deviatoric component of the minimum stress must exceed the tensile strength, known as the Terzaghi condition [e.g., Valko and Economides, 1995, p. 65]. An alternative criterion for rupture at the chamber wall sometimes considered in the literature [Grosfils, 2007; Fukushima et al., 2010] is that the minimum stress should exceed the rock tensile strength. In this case, the reservoir overpressure required for failure needs to counterbalance the lithostatic load, thus leading to reservoir overpressure above 70 MPa at 3 km depth, which is far above the values derived by interpretation of geophysical data through dynamical models for dike propagation.

### 5.3. Influence of Local Topography on Magma Path

Our models reproduce correctly the result that a topographic load tends to attract ascending dikes by deflecting their trajectory when they nucleate offset from the surface load. This is due to the deviatoric stress field induced by the load within the underlying crust. This effect provides a reliable explanation for the dike deflection observed at Etna, Italy, in July 2001 [Bonaccorso et al., 2010] and also during the late stage of the May 2008 flank eruption [Cannavò et al., 2015]. The deviatoric stress field induced beneath an edifice load may also explain the radial pattern of lateral dikes in the central part of a volcanic edifice [Roman and Jaupart, 2014]. However, it is expected that with time the deviatoric part of the stress field induced by a load applied at the surface tends to relax. After a long time, the load effect might consist in an increase of the local lithostatic pressure without any deviatoric effect. Heimisson et al. [2015] have shown that even neglecting the deviatoric component of the stress due to topography, it is possible to explain the curved pathway of the lateral dyking event of 2014 at Bardarbunga, consistently with radial dikes away from volcanic centers. Some observations of lateral dike propagation show that when the magma propagates toward a topographic maximum, it chooses to turn around it. This was the case for the Manda Hararo megadike emplaced in September 2005, which is deflected toward the east in its northern part when it would have propagated along the center of the Dabbahu volcanic edifice if following a straight line [Grandin et al., 2009, 2010]. Another example is provided by magma propagation preceding the El Hierro, Canary Islands 2011 eruption, where the path defined

by the location of seismic events turns around a submarine cone [see *Marti et al.*, 2013, Figure 1]. In these cases the deviatoric stress induced by the load may have been relaxed such that its effect is only to increase lithostatic pressure.

## 6. Conclusion

We propose the first numerical model allowing calculation of both magma trajectory and velocity. We show that both the dike orientation and velocity are controlled by the balance between the magma excess pressure (reservoir overpressure plus buoyancy forces acting along the dike) on the one hand and the local external stress field on the other hand. This model can be used to infer magma overpressure and volcanic edifice stress field from dike trajectories and magma propagation velocities derived from field observations (vent positions, co-intrusive seismic, and geodetic data). It thus represents a unique and original way to constrain the local stress field at shallow to intermediate depth on volcanoes. Once the ambient stress field is known, the model can be used to forecast in advance the magma pathway toward the surface as well as the magma ability to reach the surface. It also provides crucial additional information on the timing of the expected eruptive event. By applying our model to the July 2001 Etna eruption we showed how the magma overpressure at the dike bottom was less than 4 MPa. The proposed model can be made more complex in order to include the available information on crustal heterogeneities, local topography, and magma physical properties. Such type of deterministic dynamical models could be used in the future to assimilate in real-time geophysical data recorded by observatories during magma propagation in order to improve the forecast of the eruptive vent position and eruption timing on basaltic volcanoes such as Etna or Piton de la Fournaise.

## Acknowledgments

This work was supported by the MED-SUV Project funded by the European Union (FP7 Grant Agreement 308665) as well as PNP/INSU. We thank reviewers Thierry Menand and Roger Buck as well as Associate Editor Mark D. Behn for their suggestions, which improved the quality of the paper. The numerical code for magma propagation is available by contacting the corresponding author.

## References

- Accocella, V., and A. Tibaldi (2005), Dike propagation driven by volcano collapse: A general model tested at Stromboli, Italy, *Geophys. Res. Lett.*, 32, L0830, doi:10.1029/2004GL022248.
- Anderson, E. M. (1951), *The Dynamics of Faulting and Dike Formation With Applications to Britain*, 2nd ed., Oliver and Boyd, London.
- Benson, P. M., M. J. Heap, Y. Lavallée, A. Flaws, K.-U. Hess, A. Selvadurai, D. B. Dingwell, and B. Schillinger (2012), Laboratory simulations of tensile fracture development in a volcanic conduit via cyclic magma pressurisation, *Earth Planet. Sci. Lett.*, 349–350(0), 231–239, doi:10.1016/j.epsl.2012.07.003.
- Bonacorso, A., M. Aloisi, and M. Mattia (2002), Dike emplacement forerunning the Etna July 2001 eruption modeled through continuous tilt and GPS data, *Geophys. Res. Lett.*, 29(13), 2–1–2–4, doi:10.1029/2001GL014397.
- Bonacorso, A., G. Currenti, C. Del Negro, and E. Boschi (2010), Dike deflection modelling for inferring magma pressure and withdrawal, with application to Etna 2001 case, *Earth Planet. Sci. Lett.*, 109, 121–129, doi:10.1016/j.epsl.2010.02.030.
- Bonforte, A., S. Gambino, and M. Neri (2009), Intrusion of eccentric dikes: The case of the 2001 eruption and its role in the dynamics of Mt. Etna volcano, *Tectonophysics*, 471(1–2), 78–86, doi:10.1016/j.tecto.2008.09.028.
- Buck, W. R., P. Einarsson, and B. Brändsdóttir (2006), Tectonic stress and magma chamber size as controls on dike propagation: Constraints from the 1975–1984 Krafla rifting episode, *J. Geophys. Res.*, 111, B12404, doi:10.1029/2005JB003879.
- Cannavò, F., A. G. Camacho, P. J. González, M. Mattia, G. Puglisi, and J. Fernández (2015), Real time tracking of magmatic intrusions by means of ground deformation modeling during volcanic crises, *Sci. Rep.*, 5, 10970, doi:10.1038/srep10970.
- Chaput, M., V. Famin, and L. Michon (2013), Deformation of basaltic shield volcanoes by co-intrusive stress permutations, *J. Geophys. Res. Solid Earth*, 119, 274–301, doi:10.1002/2013JB010623.
- Corbi, F., E. Rivalta, V. Pinel, F. Maccaferri, M. Bagnardi, and V. Acocella (2015), How caldera collapse shapes the shallow emplacement and transfer of magma in active volcanoes, *Earth Planet. Sci. Lett.*, 431, 287–293, doi:10.1016/j.epsl.2015.09.028.
- Corbi, F., E. Rivalta, V. Pinel, F. Maccaferri, and V. Acocella (2016), Understanding the link between circumferential dikes and eruptive fissures around calderas based on numerical and analog models, *Geophys. Res. Lett.*, 43, 6212–6219, doi:10.1002/2016GL068721.
- Cotterell, B., and J. R. Rice (1980), Slightly curved or kinked cracks, *Int. J. of Fracture*, 16, 155–169.
- Dahm, T. (2000a), Numerical simulations of the propagation path and the arrest of fluid-filled fractures in the Earth, *Geophys. J. Int.*, 141, 623–638.
- Dahm, T. (2000b), On the shape and velocity of fluid-filled fractures in the Earth, *Geophys. J. Int.*, 142, 181–192.
- Daniels, K. A., and T. Menand (2015), An experimental investigation of dike injection under regional extensional stress, *J. Geophys. Res. Solid Earth*, 120, 2014–2035, doi:10.1002/2014JB011627.
- Del Negro, C., and G. Currenti (2003), Volcanomagnetic signals associated with the 2001 flank eruption of Mt. Etna (Italy), *Geophys. Res. Lett.*, 30(1357), doi:10.1029/2002GL015481.
- Delaney, P. T., D. D. Pollard, J. I. Ziony, and E. H. McKee (1986), Field relations between dikes and joints: Emplacement processes and paleostress analysis, *J. Geophys. Res.*, 91(B5), 4920–4938, doi:10.1029/JB091iB05p04920.
- Einarsson, P., and B. Brändsdóttir (1980), Seismological evidence for lateral magma intrusion during the 1978 deflation of the Krafla Volcano in NE Iceland, *J. Geophys.*, 47, 160–165.
- Fukushima, Y., V. Cayol, P. Durand, and D. Massonnet (2010), Evolution of magma conduits during the 1998–2000 eruptions of Piton de la Fournaise volcano, Réunion Island, *J. Geophys. Res.*, 115, B10204, doi:10.1029/2009JB007023.
- Giordano, D., and D. B. Dingwell (2003), Viscosity of hydrous Etna basalt: Implications for Plinian-style basaltic eruptions, *Bull. Volcanol.*, 65, 8–14.
- Grandin, R., et al. (2009), September 2005 Manda Hararo-Dabbahu rifting event, Afar (Ethiopia): Constraints provided by geodetic data, *J. Geophys. Res.*, 114, B08404, doi:10.1029/2008JB005843.
- Grandin, R., et al. (2010), Sequence of rifting in Afar, Manda-Hararo rift, Ethiopia, 2005–2009: Time space evolution and interactions between dikes from interferometric synthetic aperture radar and static stress change modeling, *J. Geophys. Res.*, 115, B10413, doi:10.1029/2009JB000815.

- Grosfils, E. B. (2007), Magma reservoir failure on the terrestrial planets: Assessing the importance of gravitational loading in simple elastic models, *J. Volcanol. Geotherm. Res.*, **166**, 47–75.
- Haimson, F., and B. Rummel (1982), Hydrofracturing stress measurements in the Iceland research drilling project drill hole at Reydarfjordur, Iceland, *J. Geophys. Res.*, **87**(B8), 6631–6649.
- Heimisson, E. R., A. Hooper, and F. Sigmundsson (2015), Forecasting the path of a laterally propagating dike, *J. Geophys. Res. Solid Earth*, **120**, 8774–8792, doi:10.1002/2015JB012402.
- Kühn, D., and T. Dahm (2004), Simulation of magma ascent by dikes in the mantle beneath mid-ocean ridges, *J. Geodynamics*, **38**, 147–159.
- Lawn, B. R., and T. R. Wilshaw (1975), *Fracture of Brittle Solids*, 204 pp., Cambridge Univ. Press, New York.
- Lister, J. R. (1990a), Buoyancy-driven fluid fracture: The effects of material toughness and low-viscosity precursors, *J. Fluid Mech.*, **210**, 263–280.
- Lister, J. R. (1990b), Buoyancy-driven fluid fracture: Similarity solutions for the horizontal and vertical propagation of fluid-filled cracks, *J. Fluid Mech.*, **217**, 213–239.
- Maccaferri, F., M. Bonafede, and E. Rivalta (2011), A quantitative study of the mechanisms governing dike propagation, dike arrest and sill formation, *J. Volcanol. Geotherm. Res.*, **208**, 39–50, doi:10.1016/j.jvolgeores.2011.09.001.
- Maccaferri, F., E. Rivalta, D. Keir, and V. Acocella (2014), Off-rift volcanism in rift zones determined by crustal unloading, *Nat. Geosci.*, **7**, 297–300, doi:10.1038/ngeo2110.
- Maccaferri, F., E. Rivalta, L. Passarelli, and Y. Aoki (2016), On the mechanisms governing dike arrest: Insight from the 2000 Miyakejima dike injection, *Earth Planet. Sci. Lett.*, **434**, 64–74, doi:10.1016/j.epsl.2015.11.024.
- Marti, J., V. Pinel, C. Lopez, A. Geyer, R. Abella, M. Tarraga, M. J. Blanco, A. Castro, and C. Rodriguez (2013), Causes and mechanisms of the 2011–2012 El Hierro (Canary Islands) submarine eruption, *J. Geophys. Res. Solid Earth*, **118**, 823–839, doi:10.1002/jgrb.50087.
- Martinez-Arévalo, C., D. Patane, A. Rietbroek, and J. M. Ibanez (2005), The intrusive process leading to the Mt. Etna 2001 flank eruption: Constraints from 3-D attenuation tomography, *Geophys. Res. Lett.*, **32**, L21309, doi:10.1029/2005GL023736.
- Menand, T., K. A. Daniels, and P. Benghiat (2010), Dike propagation and sill formation in a compressive tectonic environment, *J. Geophys. Res.*, **115**, B08201, doi:10.1029/2009JB006791.
- Mériaux, C., and C. Jaupart (1998), Dike propagation through an elastic plate, *J. Geophys. Res.*, **103**, 18,295–18,314.
- Mériaux, C., and J. R. Lister (2002), Calculation of dike trajectories from volcanic centres, *J. Geophys. Res.*, **107**, 1–10, doi:10.1029/2001JB00436.
- Métrich, N., P. Allard, N. Spillaert, D. Andronico, and M. Burton (2004), 2001 flank eruption of the alkali- and volatile-rich primitive basalt responsible for Mount Etna's evolution in the last three decades, *Earth Planet. Sci. Lett.*, **228**(1–2), 1–17, doi:10.1016/j.epsl.2004.09.036.
- Muller, J. R., G. Ito, and S. J. Martel (2001), Effects of volcano loading on dike propagation in an elastic half-space, *J. Geophys. Res.*, **106**, 11,101–11,113.
- Muskhelishvili, N. I. (1963), *Some Basic Problems in the Mathematical Theory of Elasticity*, 718 pp., Noordhoff, Leiden, Netherlands.
- Nakamura, K., K. H. Jacob, and J. N. Davies (1977), Volcanoes as possible indicators of tectonic stress orientation—Aleutians and Alaska, *Pure Appl. Geophys.*, **115**, 87–112.
- Patane, D., C. Chiarabba, O. Cocina, P. De Gori, M. Moretti, and E. Boschi (2002), Tomographic images and 3D earthquake locations of the seismic swarm preceding the 2001 Mt. Etna eruption: Evidence for a dike intrusion, *Geophys. Res. Lett.*, **29**(10), 135–1–135–4, doi:10.1029/2001GL014391.
- Pedersen, R., F. Sigmundsson, and P. Einarsson (2006), Controlling factors on earthquake swarms associated with magmatic intrusions: Constraints from Iceland, *J. Volcanol. Geotherm. Res.*, **162**(1–2), 73–80.
- Peltier, A., T. Staudacher, and P. Bachéléry (2007), Constraints on magma transfers and structures involved in the 2003 activity at Piton de la Fournaise from displacement data, *J. Geophys. Res.*, **112**, B03207, doi:10.1029/2006JB004379.
- Pinel, V., and C. Jaupart (2000), The effect of edifice load on magma ascent beneath a volcano, *Philos. Trans. R. Soc. London, Series A*, **358**, 1515–1532.
- Pinel, V., and C. Jaupart (2004), Magma storage and horizontal dike injection beneath a volcanic edifice, *Earth Planet. Sci. Lett.*, **221**, 245–262, doi:10.1016/j.epsl.2004.01.031.
- Rivalta, E. (2010), Evidence that coupling to magma chambers controls the volume history and velocity of laterally propagating intrusions, *J. Geophys. Res.*, **115**, B07203, doi:10.1029/2009JB006922.
- Rivalta, E., B. Taisne, A. Bunger, and R. Katz (2015), A review of mechanical models of dike propagation: Schools of thought, results and future directions, *Tectonophysics*, **638**, 1–42, doi:10.1016/j.tecto.2014.10.003.
- Roman, A., and C. Jaupart (2014), The impact of a volcanic edifice on intrusive and eruptive activity, *Earth Planet. Sci. Lett.*, **408**, 1–8, doi:10.1016/j.epsl.2014.09.016.
- Roper, S. M., and J. R. Lister (2007), Buoyancy-driven crack propagation: The limit of large fracture toughness, *J. Fluid Mech.*, **580**, 359–380.
- Roult, G., A. Peltier, B. Taisne, T. Staudacher, V. Ferrazini, A. Di Muro, and the OPVF team (2012), A new comprehensive classification of the Piton de la Fournaise activity spanning the 1985–2010 period. Search and analysis of short-term precursors from a broad-band seismological station, *J. Volcanol. Geotherm. Res.*, **241**–**242**, 78–104.
- Sigmundsson, F., et al. (2010), Intrusion triggering of the 2010 Eyjafjallajökull explosive eruption, *Nature*, **468**, 426–430, doi:10.1038/nature09558.
- Sigmundsson, F., et al. (2014), Segmented lateral dike growth in a rifting event at Bárðarbunga volcanic system, Iceland, *Nature*, **517**(7533), 191–195.
- Sneddon, I. N. (1951), *Fourier Transforms*, 542 pp., McGraw-Hill, New York.
- Taisne, B., and C. Jaupart (2009), Dike propagation through layered rocks, *J. Geophys. Res.*, **114**, B09203, doi:10.1029/2008JB006228.
- Taisne, B., and C. Jaupart (2011), Magma expansion and fragmentation in a propagating dike, *Earth Planet. Sci. Lett.*, **301**, 146–152, doi:10.1016/j.epsl.2010.10.038.
- Traversa, P., V. Pinel, and J.-R. Grasso (2010), A constant influx model for dike propagation: Implications for magma reservoir dynamics, *J. Geophys. Res.*, **115**, B01201, doi:10.1029/2009JB006559.
- Valko, P., and M. J. Economides (1995), *Hydraulic Fracture Mechanics*, 298 pp., John Wiley, London.

- Watanabe, T., T. Koyaguchi, and T. Seno (1999), Tectonic stress controls on ascent and emplacement of magmas, *J. Volcanol. Geotherm. Res.*, 91, 65–78.
- Watanabe, T., T. Masuyama, K. Nagaoka, and T. Tahara (2002), Analog experiments on magma-filled cracks: Competition between external stresses and internal pressure, *Earth Planet. Sci. Lett.*, 54, 1247–1261.
- Xu, W., J. Ruch, and S. Jonsson (2015), Birth of two volcanic islands in the southern Red Sea, *Nat Commun.*, 6, 7104.
- Zhang, X., A. P. Bunger, and R. G. Jeffrey (2014), Mechanics of two interacting magma-driven fractures: A numerical study, *J. Geophys. Res. Solid Earth*, 119, 8047–8063, doi:10.1002/2014JB011273.